Differentiable Gaussian Representation for Incomplete CT Reconstruction

Shaokai Wu¹, Yuxiang Lu¹, Wei Ji², Suizhi Huang¹, Fengyu Yang³, Shalayiding Sirejiding¹, Qichen He¹, Jing Tong¹, Yanbiao Ji¹, Yue Ding¹, Hongtao Lu¹

¹Shanghai Jiao Tong University, ²National University of Singapore, ³Yale University

Abstract

Incomplete Computed Tomography (CT) benefits patients by reducing radiation exposure. However, reconstructing high-fidelity images from limited views or angles remains challenging due to the ill-posed nature of the problem. Deep Learning Reconstruction (DLR) methods have shown promise in enhancing image quality, but the paradox between training data diversity and high generalization ability remains unsolved. In this paper, we propose a novel Gaussian Representation for Incomplete CT Reconstruction (GRCT) without the usage of any neural networks or full-dose CT data. Specifically, we model the 3D volume as a set of learnable Gaussians, which are optimized directly from the incomplete sinogram. Our method can be applied to multiple views and angles without changing the architecture. Additionally, we propose a differentiable Fast CT Reconstruction method for efficient clinical usage. Extensive experiments on multiple datasets and settings demonstrate significant improvements in reconstruction quality metrics and high efficiency. We plan to release our code as open-source.

Introduction

Computed Tomography (CT) has evolved into an essential tool in medical imaging since its inception in the 1970s, playing a pivotal role in disease diagnosis, surgical guidance, and treatment response monitoring (Zhu et al. 2018; Brenner et al. 2001; Szczykutowicz et al. 2022). However, the radiation dose associated with CT imaging presents a substantial risk to patients. In response to patient concerns about radiation exposure, Incomplete CT has emerged as a promising solution (Ma et al. 2023; Lahiri et al. 2023). This technique uses fewer views or angles to capture X-ray projections (Figure 1), thereby reducing the radiation dose to which patients are exposed (Wu et al. 2021; Fahrig et al. 2006). Not only does this method mitigate the risks associated with radiation exposure, but it also enhances the overall patient experience during medical imaging procedures.

The essence of incomplete CT is to reconstruct the 3D volume of the patient using fewer views or angles of CT projection data (formally known as sinogram). As illustrated in Figure 1, Sparse-View CT limits the number of X-ray beams, while Limited-Angle CT constrains the angle of X-ray beams, both of which are ill-posed problems. Currently, deep learning reconstruction (DLR) methods dominate this

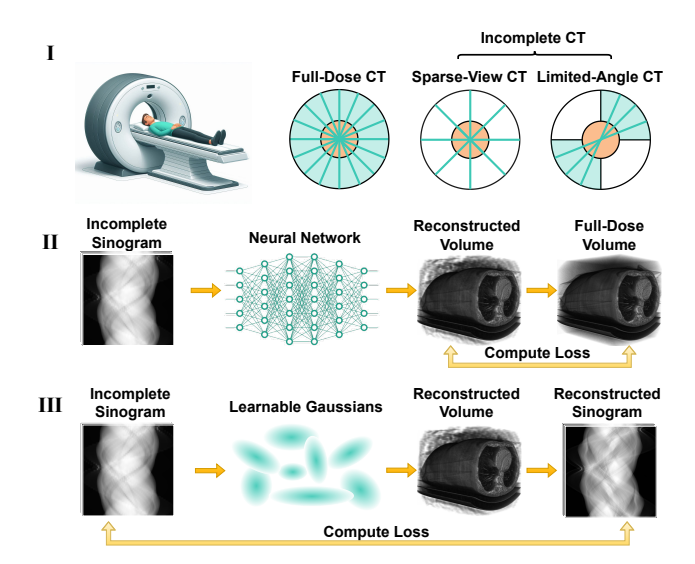


Figure 1: I, Illustration of CT scanning process and two paradigms of Incomplete CT: Sparse-View CT and Limited-Angle CT. II, deep-learning reconstruction (DLR) methods, which learn to reconstruct the volume under the supervision of Full-Dose data. III, Our proposed Gaussian Representation for CT Reconstruction (GRCT), directly optimizing a set of learnable Gaussians under the supervision of only incomplete sinograms, i.e., without Full-Dose data.

task, typically learning to reconstruct the 3D volume under the supervision of full-dose volume data. These methods vary widely, from pure image-domain denoising methods (Jin et al. 2017; Chen et al. 2017), to dual-domain methods that leverage information from both sinogram and image domains (Hu et al. 2020), and cutting-edge diffusion-based methods (Chung et al. 2022, 2023; Xu et al. 2024). However, despite the promising advancements in incomplete CT reconstruction, the clinical application of DLR methods remains limited, and patients rarely benefit from the reduced radiation dose in real-time. We summarize the challenges of incomplete CT reconstruction as follows:

Firstly, the requirement for full-dose CT data for training neural networks is a significant limitation. Regardless of the dataset size, it is impossible to cover all possible scenarios in clinical practice. The diversity in scanning data, including different radiation views or angles, patient ages, body parts, and imaging protocols, makes it challenging to collect a comprehensive dataset (Moen et al. 2021).

Secondly, the versatility of neural networks in handling multiple views and angles within a single architecture is limited. Current methods are designed for specific views and angles, such as 60-view CT, 120-view CT, 90° CT, etc., and are not easily adaptable to other views or angles. When the views or angles change, the neural networks need to be retrained, which is time-consuming and labor-intensive (Yang et al. 2022).

Thirdly, the computational complexity during the deployment stage remains high, making it less efficient for real-time applications (Koetzier et al. 2023). Advanced diffusion-based methods (Chung et al. 2022, 2023; Xu et al. 2024) can achieve a PSNR of over 45 dB, but their computational cost is also high, rendering them unsuitable for real-time applications. Furthermore, the lack of patient-specific adaptation in current methods hinders their ability to provide tailored reconstruction for each patient. As anticipated by (Szczykutowicz et al. 2022), future CT reconstruction methods should be capable of learning in real-time and adaptively updating parameters for specific patients.

Numerous challenges drive us to rethink the representation of the CT reconstruction problem. Do we need neural networks to learn the mapping from the sinogram domain to the image domain? Can we directly learn the 3D volume from the sinogram domain without full-dose CT data? Can we design a method that can be applied to multiple views and angles without changing the architecture? Can we design a method that is highly efficient for training and deployment? Can we design a method that can provide tailored reconstruction for each patient? To this end, our ideas began to surface gradually. We made a bold attempt: to abandon the classic neural network architecture and instead use a set of Gaussians to represent CT scenes. This motivation is inspired by the 3D Gaussian Splatting (3DGS) (Kerbl et al. 2023) method in neural graphics, which has shown great potential for reconstructing 3D scenes with a set of Gaussians. However, we are not satisfied with the current 3DGS on incomplete CT, as it is not designed for the medical imaging domain and lacks a direct reconstruction process for the entire volume. Instead, we designed a novel Gaussian Representation as well as a Fast CT Reconstruction method. Our representation is differentiable, and our reconstruction process is highly parallelized, allowing for end-to-end training. Our method can be applied to multiple views and angles without changing the architecture. We extensively evaluate our method under multiple settings of incomplete CT reconstruction to demonstrate that it can achieve significant improvements in both reconstruction quality metrics and efficiency.

The main contributions of this paper are as follows:

- We propose a novel Gaussian Representation for Incomplete CT Reconstruction (GRCT). This method directly learns to reconstruct the 3D volume from Gaussian functions within the current patient's sinogram domain, regardless of the number of views or angles acquired.
- · We provide a Fast CT Reconstruction method that com-

- bines the contributions of the Gaussians in a highly parallel manner into a discretized volume, where the whole process is differentiable and end-to-end.
- We conduct extensive experiments in multiple settings to demonstrate the effectiveness of our method in improving reconstruction quality metrics and efficiency.

Related Work

CT reconstruction techniques have significantly evolved from traditional algorithms to deep learning methods. Below, we recap its development and focus on the incomplete CT reconstruction problem.

Traditional methods CT reconstruction methods began with algebraic reconstruction (ART) (Herman, Lent, and Rowland 1973) and have since evolved to Filtered Back Projection (FBP) (Bracewell and Riddle 1967; Kak and Slaney 2001; Willemink and Noël 2019), which is now the standard in clinical practice due to its simplicity and efficiency. However, FBP struggles with inherent noise in raw data, especially at lower doses (Szczykutowicz et al. 2022), leading to grainy images that obscure subtle tissue variations.

To strike a balance between ionizing radiation exposure and image quality, iterative reconstruction (IR) methods were developed (Gordon, Bender, and Herman 1970; Andersen and Kak 1984; Nuyts, Michel, and Dupont 2001; Hudson and Larkin 1994). These methods leverage optimization algorithms such as maximum likelihood expectation maximization (Nuyts, Michel, and Dupont 2001) and ordered subset expectation maximization (Hudson and Larkin 1994). Despite their effectiveness, their computational demands and slow convergence make them impractical for real-time applications.

Deep Learning methods The challenges above led to the development of Deep Learning CT Reconstruction (DLR) methods (Szczykutowicz et al. 2022; Koetzier et al. 2023), which excel in addressing challenges like noise reduction, artifact suppression, and image quality enhancement. DLR methods (Zhu et al. 2018; Jin et al. 2017; Chen et al. 2017; Hu et al. 2020; Lee, Lee, and Cho 2017; Su et al. 2022; Zhang et al. 2017) can be divided into two main categories: direct and indirect learning (Koetzier et al. 2023; Yang et al. 2022). Direct learning methods train a network to reconstruct images directly from sinograms, with examples being AUTOMAP (Zhu et al. 2018), which uses manifold approximation, and iRadonMAP (He, Wang, and Ma 2020), which leverages learnable filtering and back-projection. Indirect learning methods (Jin et al. 2017; Kang, Min, and Ye 2017; Han and Ye 2018; Chen et al. 2017), on the other hand, treat CT reconstruction as a high-level denoising problem, processing raw sinogram data through FBP or IR to the image domain, and aim to train a network to map from incomplete to full-dose sinograms or images.

Preliminary

Problem Formulation Clinical CT imaging involves capturing X-ray projections of the patient from various angles, which are then processed to reconstruct a 3D volume representing the internal structures of the patient. For simplicity,

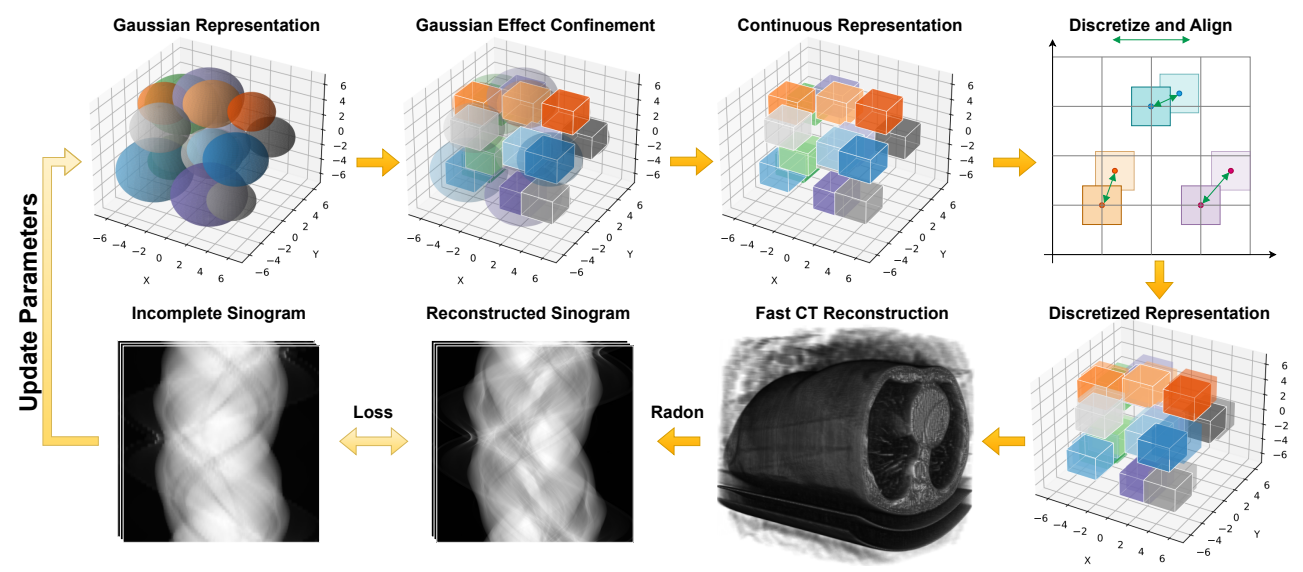


Figure 2: Framework of our Gaussian Representation for Computed Tomography (GRCT).

we start the problem formulation from the 2D condition. The CT imaging process for a 2D image slice is described by:

$$y = Ax + \beta, \tag{1}$$

where $x \in \mathbb{R}^{w \times h}$ represents the 2D image with width w and height $h, y \in \mathbb{R}^{m \times n}$ is the sinogram matrix with m representing the number of projection views and n the number of detector elements per view. The matrix $A \in \mathbb{R}^{m \times n \times w \times h}$ represents the Radon Transform matrix, a sparse matrix that maps the geometric relationship between the object and the X-ray source/detector system. It describes how the attenuation along various paths within the object contributes to the intensity measured at each detector element for every projection view. Lastly, $\beta \in \mathbb{R}^{m \times n}$ represents the noise term in the system.

Mathematically, the Radon Transform matrix A can be thought of as a collection of line integrals. Each element of A corresponds to a specific line (or path) through the image x, from a specific projection angle. The value of each element of A is the sum of the pixel values along its corresponding line in the image. In other words, each element of A represents the total attenuation of the X-rays along a specific path through the object. In mathematical terms, if we denote the image as a function f(x,y), the Radon Transform $Rf(\rho,\theta)$ at a distance ρ from the origin and an angle θ is given by:

$$Rf(\rho,\theta) = \int_{-\infty}^{\infty} f(\rho\cos\theta - t\sin\theta, \rho\sin\theta + t\cos\theta)dt.$$

Sparse-View CT Reconstruction In Sparse-View CT, the number of projection views m_s is reduced compared to the full-dose set:

$$y = A_s x + \beta, \tag{3}$$

$$A_s = A[I_{m_s}], \ I_{m_s} \subset \{1, 2, \dots, m\},$$
 (4)

with these views typically being evenly distributed across the angular space in most practices (Zhu et al. 2018; Jin et al. 2017; Chen et al. 2017),

Limited-Angle CT Reconstruction Limited-Angle CT captures projection views over a restricted angular range, which can be less than 180 degrees. This limitation leads to projection data lacking crucial information from certain directions, potentially introducing artifacts into the reconstructed image:

$$y = A_l x + \beta, \tag{5}$$

$$A_l = A[I_{m_l}], I_{m_l} = i, i+1, \dots, i+m_l-1,$$
 (6)

where m_l specifies the number of projection views.

Methodology

We illustrate our GRCT framework in Figure 2. Our method begins with the proposed CT Gaussian Representation, which models the 3D volume as a set of learnable Gaussians within a central contribution box. These Gaussians are discretized into a 3D grid, aligning their contributions to directly reconstruct the entire volume. We then introduce our Fast CT Reconstruction method, which efficiently combines the contributions of the Gaussians into a discretized volume in a highly parallelized manner. The entire process is differentiable and end-to-end trainable. Additionally, we detail the optimization strategy used to update the Gaussian parameters and the loss function defined in the sinogram space.

CT Gaussian Representation

Basic Formulation We define Gaussian function centered at μ with covariance Σ as:

$$G(x, \mu, \Sigma) = e^{-\frac{1}{2}(x-\mu)^{\top} \Sigma^{-1}(x-\mu)},$$
 (7)

where $x \in \mathbb{R}^d$ is the 3D point in the scene. Characterized by a bell-shaped curve, the Gaussian function is symmetric around the mean μ with a standard deviation σ that dictates its spread in 3D space. For CT reconstruction, we use a set of Gaussians to represent the entire 3D volume:

$$L_{CT}(x, \theta, \phi) = \sum_{i} G(x, \mu_i, \Sigma_i) \cdot I_i, \tag{8}$$

where I_i is the intensity of the *i*-th Gaussian, which serves as the intensity of the voxel in the volume, and also the weight of the Gaussian. The expression $(x-\mu)^{\top}\Sigma^{-1}(x-\mu)$ is known as the squared Mahalanobis distance, denoted as D^2 in the following sections.

Gaussian Effect Confinement We restrict the contribution of each Gaussian to a local region surrounding each voxel. This is based on the principle that a Gaussian's impact on a voxel diminishes with increasing distance from the Gaussian center to the voxel. By only considering the contributions of Gaussians within a specified proximity of each voxel, we can accelerate the reconstruction process. We define the local region around each voxel as a rectangular box $B \in \mathbb{R}^{w_0 \times h_0 \times c_0}$ centered on the voxel, where w_0 , h_0 , and c_0 denote the size of the box, and are restricted to odd numbers to center the box on a voxel.

Another benefit of utilizing a local region is that $B'=B-\mu$ remains constant for all voxels within the box, allowing for precomputation. The x-coordinate range within the box spans $[-\frac{w_0-1}{2},\frac{w_0-1}{2}]$, with y and z ranges following similarly. The squared Mahalanobis distance D^2 between the voxel and the Gaussian's mean can be computed as:

$$D^2 = B'^T C^{-1} B'. (9)$$

The contribution of *i*-th Gaussian at μ_i to the volume is:

$$e^{-\frac{1}{2}D^2} \cdot I_i$$
. (10)

Interestingly, this contribution within the local region is irrelevant to the Gaussian's center position μ . This is because each point in B has coordinates centered around μ . Subtracting μ from B eliminates μ , making B' independent of μ . Mathematically, the Gaussian function's shape remains invariant under translation; shifting μ changes the peak's location but not the function's overall shape.

Discretize and Align Directly using μ for indexing and summing all Gaussian contributions would prevent the gradient of μ from passing through the sum operation. This arises because the discretized 3D volume V is comprised of integer coordinates, whereas μ is continuous. Direct discretization of μ to the nearest integer for indexing would make the reconstruction process non-differentiable. Using interpolation to compute the contribution seems to be a solution, but it is computationally demanding and may introduce additional artifacts due to error accumulation.

To address this problem, we compute each Gaussian's contribution at the discretized grid instead of its continuous position. We choose the nearest integer to the box center as the index, with the new box centered at this integer denoted as B''. Ignoring dimensional discrepancies, the relationship between B', B'', and μ is:

$$B'' + \mu - |\mu| = B'. \tag{11}$$

For simplicity, we denote $\Delta \mu = \mu - \lfloor \mu \rfloor$. Taking the dimensions into consideration, we have:

$$B_{n,w_0,h_0,c_0,d}^{\prime\prime} = B_{w_0,h_0,c_0,d}^{\prime} - \Delta\mu_{n,1,1,1,d}, \qquad (12)$$

where $\Delta\mu_{n,1,1,1,d}$ implicitly denotes the expansion of $\Delta\mu_{n,d}$ to identical dimensions for element-wise subtraction.

Fast CT Reconstruction

Parallel Computation In Formula 8, the key to the fast reconstruction process lies in the computation of the squared Mahalanobis distance D^2 within the local region. According to the definition of the discretized box B'', the squared Mahalanobis distance D^2 can be computed as $D^2 = B''^T C^{-1}B''$. We use the Einstein summation convention to represent the computation of D^2 in a more specific form:

$$D_{n,w_0,h_0,c_0}^2 = \sum_d B_{n,w_0,h_0,c_0,d}^{"} C_{n,d,d}^{-1} B_{n,w_0,h_0,c_0,d}^{"}.$$
(13)

This process allows us to compute the contribution of each Gaussian within the local region around each voxel in a highly parallelized manner. The contributions of all Gaussians are then summed to obtain the final volume.

Decomposition To further reduce computation, we decompose the large Einstein summation above into four smaller Einstein summations:

$$B'^{T}C^{-1}B'_{n,w_0,h_0,c_0} = \sum_{d} B'_{w_0,h_0,c_0,d} C_{n,d,d}^{-1} B'_{w_0,h_0,c_0,d},$$
(14)

$$B'^{T}C^{-1}\Delta\mu_{n,w_{0},h_{0},c_{0}} = \sum_{d} B'_{w_{0},h_{0},c_{0},d} C_{n,d,d}^{-1} \Delta\mu_{n,1,1,d},$$
(15)

$$\Delta \mu^T C^{-1} B'_{n,w_0,h_0,c_0} = \sum_d \Delta \mu_{n,1,1,d} C_{n,d,d}^{-1} B'_{w_0,h_0,c_0,d},$$
(16)

$$\Delta \mu^T C^{-1} \Delta \mu_{n,1,1,1} = \sum_d \Delta \mu_{n,1,1,d} \ C_{n,d,d}^{-1} \ \Delta \mu_{n,1,1,d},$$
(17)

and the final contribution of Gaussians can be computed as:

$$\Gamma = e^{-\frac{1}{2}(B'^T C^{-1} B' + B'^T C^{-1} \Delta \mu + \Delta \mu^T C^{-1} B' + \Delta \mu^T C^{-1} \Delta \mu)} \cdot I,$$
(18)

where $\Gamma \in \mathbb{R}^{n \times w_0 \times h_0 \times c_0}$ denotes the contributions of the Gaussians within the local region. This decomposition allows us to compute the contributions of the Gaussians in a more efficient manner, which significantly reduces time complexity while maintaining overall space complexity. Table 8 provides quantitative evidence of this efficiency boost. The key to this improvement lies in the fact that the Einstein summation involves tensors of significantly smaller dimensions compared to the original one. Specifically, $B'_{w_0,h_0,c_0,d}$ is only $\frac{1}{n}$ the size of $B''_{n,w_0,h_0,c_0,d}$, enabling far more efficient computations.

Once we compute the Gaussian contributions within a local region, we can sum them to obtain the final volume:

$$V_{x,y,z} \leftarrow V_{x,y,z} + \Gamma_{i,x,y,z}. \tag{19}$$

Importantly, these operations can be performed in parallel for all voxels in the volume, making the process highly efficient. Considering its practicality is stronger than the theoretical aspect, we include the detailed implementation in supplementary materials for interested readers.

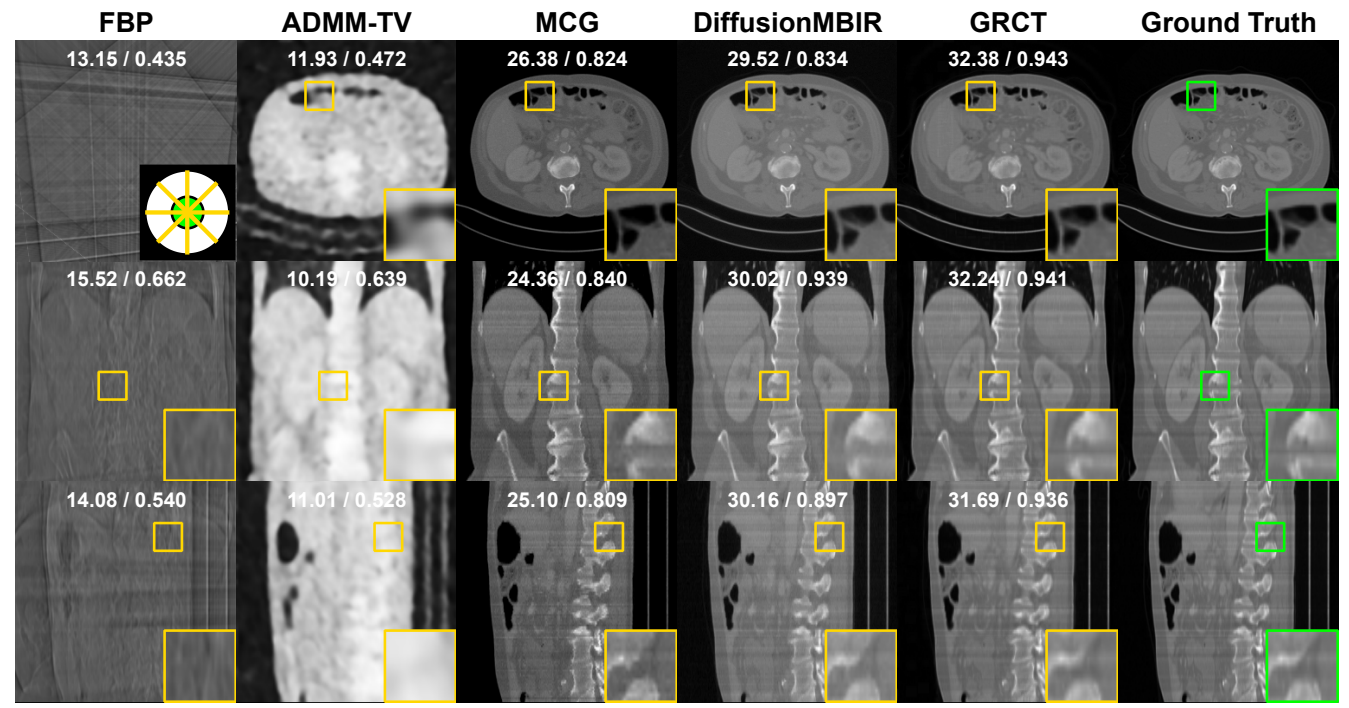


Figure 3: Visualization of Different Methods for 4-view SVCT Reconstruction. First Row: Axial View, Second Row: Coronal View, Third Row: Sagittal View. Regions in the boxes are zoomed in at the bottom-right corner.

Post Processing After reconstructing the 3D volume from the Gaussians, we aim to optimize the parameters of the Gaussians in the sinogram space. The first step is to project the 3D volume back to the sinogram space using the Radon Transform. We project the 3D volume V to the sinogram space using the Radon Transform matrix A:

$$\hat{S} = A \cdot V,\tag{20}$$

where $\hat{S} \in \mathbb{R}^{m \times n \times p}$ is the estimated sinogram.

Then we optimize the parameters of the Gaussians to minimize the discrepancy between the estimated sinogram \hat{S} and the reference incomplete sinogram S, guided by a simple L2 norm loss:

$$\mathcal{L} = \frac{1}{2} ||\hat{S} - S||_2^2. \tag{21}$$

The entire process is differentiable, allowing us to back-propagate the gradients through the entire pipeline to update the parameters of the Gaussians in an end-to-end manner. This completes the incomplete CT reconstruction and Gaussian optimization, and the process can be repeated iteratively to refine the reconstruction quality.

Experiments

We present extensive experiments on incomplete CT reconstruction using the AAPM-Mayo LDCT (Moen et al. 2021) and FUMPE (Masoudi et al. 2018) datasets. Notably, many CT reconstruction methods lack standardized protocols, including view number selection and evaluation metrics. Additionally, some methods lack public official implementations. To ensure a comprehensive and fair comparison, we

reproduce methods where possible and organize the experiments into three groups: Sparse-View CT (Tables 1 and 2), Ultra-Sparse-View CT (Tables 3, 4, and 5), and Limited-Angle CT (Table 6).

Detailed Experiment Settings

Dataset We conducted experiments using two public datasets: the AAPM-Mayo LDCT dataset (Moen et al. 2021) and the FUMPE dataset (Masoudi et al. 2018). The AAPM-Mayo LDCT dataset is widely used for incomplete CT reconstruction and comprises 2378 slices with 3mm thickness and 5388 slices with 1mm thickness. For our experiments, we focused on the 1mm thickness slices, as most recent methods evaluate using this data. The FUMPE dataset consists of 8792 chest CT images. Note that only DLR methods require full-dose sinograms or CT images for training, and the number of training data samples is listed in the tables for reference.

Compared Methods We conducted a comprehensive comparison with various methods, including denoising-based approaches (FBPConvNet (Jin et al. 2017), U-Net (Lee et al. 2018), PLANet (Yang et al. 2022), Lahiri et al. (Lahiri et al. 2023)), generative models (MCG (Chung et al. 2022), DiffusionMBIR (Chung et al. 2023), GMSD (Guan et al. 2023), SWORD (Xu et al. 2024)), NeRF-based methods (NeRP (Shen, Pauly, and Xing 2022)), and another Gaussian-based method, 3D Gaussian Splatting (Kerbl et al. 2023). Additionally, we included the traditional FBP (Bracewell and Riddle 1967; Kak and Slaney 2001) method and ADMM-TV (McCann et al. 2016) for comparison. To ensure fairness, we reproduced methods where necessary.

Table 1: Comparisons of 180/120/90/60-view SVCT on AAPM-Mayo LDCT dataset. Best in Bold.

Method	Method Training Data		180-view		120-view		90-view		view
Method	Hailing Data	PSNR	SSIM	PSNR	SSIM	PSNR	SSIM	PSNR	SSIM
FBPConvNet (TIP 17)	4839	42.23	0.988	39.45	0.983	37.11	0.976	35.63	0.966
U-Net (TRPMS 18)	4839	38.37	0.985	35.58	0.977	30.09	0.947	28.83	0.937
PLANet (ACM'MM 22)	4176	42.76	0.965	41.67	0.962	40.99	0.957	38.97	0.941
GMSD (TRPMS 23)	4839	41.44	0.988	39.41	0.981	37.25	0.974	34.31	0.958
SWORD (TMI 24)	4839	45.08	0.994	42.49	0.990	41.27	0.986	38.49	0.978
FBP	0	31.69	$-\bar{0}.\bar{8}8\bar{2}^{-}$	$\bar{28.30}$	0.787	26.20	$\bar{0.701}^{-}$	$\bar{23.18}$	0.595
NeRP (TNNLS 22)	0	37.32	0.951	36.88	0.947	37.98	0.955	37.29	0.951
3DGS (ACM'Siggraph 23)	0	41.70	0.989	41.36	0.986	40.04	0.985	38.49	0.982
GRCT (ours)	0	46.13	0.997	44.64	0.994	43.23	0.992	40.25	0.985

Table 2: Comparisons of 180/120/90/60-view SVCT on FUMPE dataset. Best in **Bold.**

Method	Training Data	180-view		120-view		90-view		60-view	
Method	Hailing Data	PSNR	SSIM	PSNR	SSIM	PSNR	SSIM	PSNR	SSIM
MCG (NeurIPS 22)	8341	36.93	0.898	37.05	0.899	37.03	0.899	35.46	0.900
DiffusionMBIR (CVPR 23)	8341	36.78	0.914	36.50	0.907	36.79	0.918	34.86	0.918
SWORD (TMI 24)	8341	41.50	0.967	39.69	0.959	37.77	0.948	31.64	0.910
FBP		33.74	0.859	30.65	0.803	$-28.\overline{5}2^{-}$	0.757	25.59	0.592
NeRP (TNNLS 22)	0	35.33	0.903	34.83	0.881	33.84	0.872	32.94	0.840
3DGS (ACM'Siggraph 23)	0	37.08	0.909	36.44	0.895	35.60	0.879	33.34	0.861
GRCT (Ours)	0	41.78	0.978	40.13	0.969	38.13	0.961	36.48	0.923

Table 3: AAPM-Mayo LDCT 8-view CT reconstruction.

	-						
Method	Data	Axial		Coronal		Sagittal	
Method	Data	PSNR ↑	SSIM ↑	PSNR ↑	SSIM ↑	PSNR ↑	SSIM ↑
FBPConvNet (TIP 17)	3142	16.57	0.553	19.12	0.774	18.11	0.714
ADMM-TV (TIP 17)	3142	16.79	0.645	18.95	0.772	17.27	0.716
MCG (NeurIPS 22)	3839	28.61	0.873	28.05	0.884	24.45	0.765
Lahiri et al. (TCI 23)	3142	21.38	0.711	23.89	0.769	20.81	0.716
DiffusionMBIR (CVPR 23)	3142	33.49	0.942	35.18	0.967	32.18	0.910
FBP	_ 0	16.31	0.320	16.65	0.320	16.34	0.322
NeRP (TNNLS 22)	0	26.96	0.648	27.05	0.655	26.99	0.650
3DGS (ACM'Siggraph 23)	0	29.91	0.896	33.27	0.893	29.71	0.918
GRCT (Ours)	0	35.54	0.956	37.05	0.954	35.65	0.956

Table 4: AAPM-Mayo LDCT 4-view CT reconstruction.

Method	Data	Axial		Coronal		Sagittal	
Method	Data	PSNR ↑	SSIM ↑	PSNR ↑	SSIM ↑	PSNR ↑	SSIM ↑
FBPConvNet (TIP 17)	3142	16.45	0.529	19.47	0.713	15.48	0.610
ADMM-TV (TIP 17)	3142	13.59	0.618	15.23	0.682	14.60	0.638
MCG (NeurIPS 22)	3839	27.33	0.855	26.52	0.863	23.04	0.745
Lahiri et al. (TCI 23)	3142	20.37	0.652	21.41	0.721	18.40	0.665
DiffusionMBIR (CVPR 23)	3142	30.52	0.914	30.09	0.938	27.89	0.871
FBP	0	13.28	0.206	13.83	0.215	13.33	0.211
NeRP (TNNLS 22)	0	20.27	0.325	20.44	0.303	20.12	0.314
3DGS (ACM'Siggraph 23)	0	26.33	0.797	28.16	0.899	26.25	0.838
GRCT (Ours)	0	30.96	0.919	31.84	0.930	31.09	0.921

Implementation Details

We implement GRCT using PyTorch and train it on a single NVIDIA A40 GPU. We set the number of Gaussians to 150K at initialization and the size of the local box to $17 \times 17 \times 17$. We use the Adam optimizer with a learning rate of 3e-4 and decay to 3e-5 at the end of training. For 2-view, 4-view, and 8-view Ultra SVCT, we set the training iteration to 1K, 2K, and 3K, respectively. For SVCT and LACT, we set the training iteration to 30K. We use the same evaluation

Table 5: AAPM-Mayo LDCT 2-view CT reconstruction.

	-						
Method	Data		Axial		Coronal		ittal
Wellou	Data	PSNR ↑	SSIM ↑	PSNR ↑	SSIM ↑	PSNR ↑	SSIM ↑
FBPConvNet (TIP 17)	3142	16.31	0.521	17.05	0.521	11.07	0.483
ADMM-TV (TIP 17)	3142	10.28	0.409	13.77	0.616	11.49	0.553
MCG (NeurIPS 22)	3839	24.69	0.821	23.52	0.806	20.71	0.685
Lahiri et al. (TCI 23)	3142	19.74	0.631	19.92	0.720	17.34	0.650
DiffusionMBIR (CVPR 23)	3142	24.11	0.810	23.15	0.841	21.72	0.766
FBP		8.81	0.142	10.30	0.159	8.89	0.147
NeRP (TNNLS 22)	0	19.69	0.277	19.72	0.280	19.62	0.270
3DGS (ACM'Siggraph 23)	0	20.58	0.545	22.28	0.618	20.69	0.513
GRCT (Ours)	0	24.06	0.778	25.46	0.815	24.12	0.780

metrics as the previous methods, including PSNR and SSIM, which are calculated between the reconstructed volume and the ground truth volume.

Sparse-View CT Reconstruction

We first evaluate GRCT on Sparse-View CT reconstruction in Table 1 and Table 2, where the number of views is reduced to 180, 120, 90, and 60. GRCT achieves the best performance in terms of PSNR and SSIM across all view numbers. On both datasets, GRCT outperforms the second-best method SWORD by a large margin, demonstrating the effectiveness of GRCT in Sparse-View CT reconstruction. It is worth noting that GRCT does not need full-dose training data while achieving superior performance. Compared to another heated Gaussian-based method 3DGS, GRCT also demonstrates a better performance.

Ultra-Sparse-View CT Reconstruction

We further evaluate GRCT on Extreme Sparse-View CT reconstruction, where the number of views is reduced to 8, 4, and 2. We present the results in Table 3, Table 4, and Table 5. GRCT achieves the best performance in terms of PSNR and

Table 6: AAPM-Mayo LDCT 90° LACT reconstruction.

Method	Doto	Axial		Coronal		Sagittal	
Method	Data -	PSNR ↑	SSIM ↑	PSNR ↑	SSIM ↑	PSNR ↑	SSIM ↑
FBPConvNet (TIP 17)	3142	26.76	0.879	25.77	0.874	22.92	0.841
ADMM-TV (TIP 17)	3142	23.19	0.793	22.96	0.758	19.95	0.782
MCG (NeurIPS 22)	3839	26.01	0.838	24.55	0.823	21.59	0.706
Lahiri et al. (TCI 23)	3142	28.08	0.931	26.02	0.856	23.24	0.812
DiffusionMBIR (CVPR 23)	3142	34.92	0.956	32.48	0.947	28.82	0.832
FBP	0	14.91	0.397	17.07	0.411	15.46	0.403
NeRP (TNNLS 22)	0	31.03	0.878	31.54	0.871	31.34	0.866
3DGS (ACM'Siggraph 23)	0	32.77	0.927	35.35	0.922	32.24	0.946
GRCT (Ours)	0	38.22	0.970	39.32	0.969	38.35	0.970

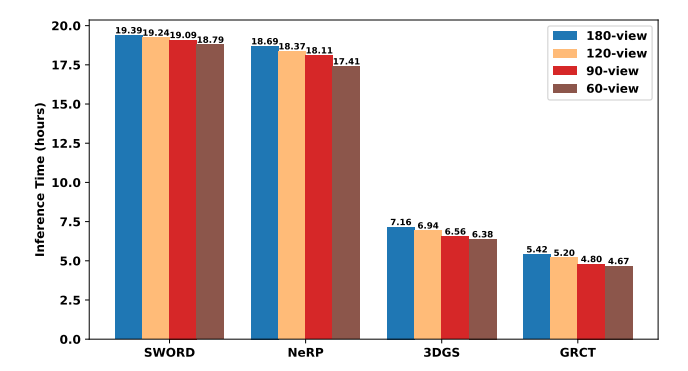


Figure 4: Computational Efficiency of Different Methods

SSIM across all view numbers. Specifically, GRCT achieves a PSNR of 35.54 and an SSIM of 0.956 with 8 views, which outperforms the two diffusion-based methods DiffusionM-BIR and MCG. In more extreme cases of 4 and 2 views, there is an obvious decrease in performance for all methods. Nevertheless, GRCT is still competitive in this condition, demonstrating its robustness to Ultra Sparse-View CT reconstruction. Moreover, it is worth noting that GRCT has a relatively stable performance across axial, coronal, and sagittal views, which shows its versatility in different viewing angles. In Figure 3, we present visual comparisons of various methods employed for 4-view SVCT reconstruction. We include more visual performance evaluations in supplementary materials for interested readers.

Limited-Angle CT Reconstruction

Then we evaluate GRCT on Limited-Angle CT reconstruction, where the projection data is acquired within a 90° range out of 180°. We compare GRCT with several advanced methods, other settings remain the same as Extreme Cases of Sparse-View CT reconstruction. Our GRCT achieves the best performance on all metrics across axial, coronal, and sagittal views without bells and whistles. Specifically, GRCT achieves a PSNR of 38.22 and an SSIM of 0.970, which outperforms the second-best method DiffusionMBIR by a large margin. This demonstrates the effectiveness of GRCT in Limited-Angle CT reconstruction.

Computational Efficiency

We compare the total time consumption of GRCT with three types of most advanced methods, including diffusion model SWORD, NeRF-based method NeRP, and 3D Gaussian Splatting. We present the results in Figure 4. Benefitting

Table 7: Effect of Box Size on 60-view SVCT

Box-Size	$13\times13\times13$	$15\times15\times15$	$17\times17\times17$	$19\times19\times19$
Time (h)	1.32	1.85	2.77	4.51
V-Ram (GiB)	10.70	13.29	16.87	21.32
PSNR / SSIM	35.99 / 0.960	38.90 / 0.973	40.25 / 0.985	40.98 / 0.987

Table 8: Video-Memory and Time Per Iteration

Method	VRAM (GiB)	Time (s)
Direct Fast w/o decomposition Fast w/ decomposition	16662.50 16.87 16.87	/ 1.05 0.09

from our Fast CT Reconstruction, GRCT achieves the lowest time consumption across all methods, demonstrating its high computational efficiency.

Ablation Study

Effect of Box Size In Table 7, we evaluate the effect of the box size on 60-view SVCT on AAPM-Mayo LDCT. We observe that the performance increases as the box size increases, which is because the larger box size provides more context information for the optimization of Gaussians. However, the time consumption and video memory also increase with the box size. We choose $17 \times 17 \times 17$ as the default box size in our experiments, which achieves a good balance between performance and efficiency.

Effect of Fast CT Reconstruction We compare the video-memory and time consumption of the Direct reconstruction and the Fast CT Reconstruction in Table 8. We observe that the Fast CT Reconstruction achieves a significant reduction in time consumption compared to the Direct reconstruction. The decomposition further reduces the time consumption from 1.05s to 0.09s, which enables the efficient reconstruction of GRCT.

Effect of View and Angle Selection In Table 1 - Table 6, the results show different performance under multiple views and limited angles. We observe that GRCT achieves the best performance when the number of views is 180, and the performance decreases as the number of views decreases in SVCT. This is because the sinogram acquired from more views provides more information about the attenuation distribution that helps to improve the reconstruction quality. The performance of LACT is better than the 8-view SVCT but worse than the 60-view SVCT because the limited angle leads to a loss of information from certain views. In all groups, GRCT achieves superior performance while not needing any high-dose data for training.

Conclusion

In this paper, we propose GRCT to represent the volume as a set of 3D Gaussians and optimize their parameters to align the estimated and incomplete sinograms. Besides, we propose a Fast CT Reconstruction process to parallelize the optimization of Gaussians and achieve efficient reconstruction. Extensive experiments on Incomplete CT reconstruction shows GRCT's state-of-the-art performance and low computational cost, highlighting the potential of Gaussian Representation for efficient, tailored LDCT reconstruction.

References

- Andersen, A. H.; and Kak, A. C. 1984. Simultaneous algebraic reconstruction technique (SART): a superior implementation of the ART algorithm. *Ultrasonic imaging*, 6(1): 81–94.
- Bracewell, R. N.; and Riddle, A. 1967. Inversion of fanbeam scans in radio astronomy. *Astrophysical Journal, vol.* 150, p. 427, 150: 427.
- Brenner, D. J.; Elliston, C. D.; Hall, E. J.; and Berdon, W. E. 2001. Estimated risks of radiation-induced fatal cancer from pediatric CT. *American journal of roentgenology*, 176(2): 289–296.
- Chen, H.; Zhang, Y.; Kalra, M. K.; Lin, F.; Chen, Y.; Liao, P.; Zhou, J.; and Wang, G. 2017. Low-dose CT with a residual encoder-decoder convolutional neural network. *IEEE transactions on medical imaging*, 36(12): 2524–2535.
- Chung, H.; Ryu, D.; Mccann, M. T.; Klasky, M. L.; and Ye, J. C. 2023. Solving 3d inverse problems using pre-trained 2d diffusion models. IEEE. In *CVF Conference on Computer Vision and Pattern Recognition*, volume 1, 6.
- Chung, H.; Sim, B.; Ryu, D.; and Ye, J. C. 2022. Improving diffusion models for inverse problems using manifold constraints. *Advances in Neural Information Processing Systems*, 35: 25683–25696.
- Fahrig, R.; Dixon, R.; Payne, T.; Morin, R. L.; Ganguly, A.; and Strobel, N. 2006. Dose and image quality for a conebeam C-arm CT system. *Medical physics*, 33(12): 4541–4550.
- Gordon, R.; Bender, R.; and Herman, G. T. 1970. Algebraic reconstruction techniques (ART) for three-dimensional electron microscopy and X-ray photography. *Journal of theoretical Biology*, 29(3): 471–481.
- Guan, B.; Yang, C.; Zhang, L.; Niu, S.; Zhang, M.; Wang, Y.; Wu, W.; and Liu, Q. 2023. Generative modeling in sinogram domain for sparse-view CT reconstruction. *IEEE Transactions on Radiation and Plasma Medical Sciences*.
- Han, Y.; and Ye, J. C. 2018. Framing U-Net via deep convolutional framelets: Application to sparse-view CT. *IEEE transactions on medical imaging*, 37(6): 1418–1429.
- He, J.; Wang, Y.; and Ma, J. 2020. Radon inversion via deep learning. *IEEE transactions on medical imaging*, 39(6): 2076–2087.
- Herman, G. T.; Lent, A.; and Rowland, S. W. 1973. ART: mathematics and applications: a report on the mathematical foundations and on the applicability to real data of the algebraic reconstruction techniques. *Journal of theoretical biology*, 42(1): 1–32.
- Hu, D.; Liu, J.; Lv, T.; Zhao, Q.; Zhang, Y.; Quan, G.; Feng, J.; Chen, Y.; and Luo, L. 2020. Hybrid-domain neural network processing for sparse-view CT reconstruction. *IEEE Transactions on Radiation and Plasma Medical Sciences*, 5(1): 88–98.
- Hudson, H. M.; and Larkin, R. S. 1994. Accelerated image reconstruction using ordered subsets of projection data. *IEEE transactions on medical imaging*, 13(4): 601–609.

- Jin, K. H.; McCann, M. T.; Froustey, E.; and Unser, M. 2017. Deep convolutional neural network for inverse problems in imaging. *IEEE transactions on image processing*, 26(9): 4509–4522.
- Kak, A. C.; and Slaney, M. 2001. Principles of computerized tomographic imaging. SIAM.
- Kang, E.; Min, J.; and Ye, J. C. 2017. A deep convolutional neural network using directional wavelets for low-dose X-ray CT reconstruction. *Medical physics*, 44(10): e360–e375.
- Kerbl, B.; Kopanas, G.; Leimkühler, T.; and Drettakis, G. 2023. 3d gaussian splatting for real-time radiance field rendering. *ACM Transactions on Graphics*, 42(4): 1–14.
- Koetzier, L.; Mastrodicasa, D.; Szczykutowicz, T.; Werf, N.; Wang, A.; Sandfort, V.; van der Molen, A.; Fleischmann, D.; and Willemink, M. 2023. Deep Learning Image Reconstruction for CT: Technical Principles and Clinical Prospects. *Radiology*, 306.
- Lahiri, A.; Maliakal, G.; Klasky, M. L.; Fessler, J. A.; and Ravishankar, S. 2023. Sparse-view cone beam ct reconstruction using data-consistent supervised and adversarial learning from scarce training data. *IEEE Transactions on Computational Imaging*, 9: 13–28.
- Lee, H.; Lee, J.; and Cho, S. 2017. View-interpolation of sparsely sampled sinogram using convolutional neural network. In *Medical Imaging 2017: Image Processing*, volume 10133, 617–624. SPIE.
- Lee, H.; Lee, J.; Kim, H.; Cho, B.; and Cho, S. 2018. Deepneural-network-based sinogram synthesis for sparse-view CT image reconstruction. *IEEE Transactions on Radiation and Plasma Medical Sciences*, 3(2): 109–119.
- Ma, C.; Li, Z.; He, J.; Zhang, J.; Zhang, Y.; and Shan, H. 2023. Universal Incomplete-View CT Reconstruction with Prompted Contextual Transformer. *arXiv preprint arXiv:2312.07846*.
- Masoudi, M.; Pourreza, H.-R.; Saadatmand-Tarzjan, M.; Eftekhari, N.; Zargar, F. S.; and Rad, M. P. 2018. A new dataset of computed-tomography angiography images for computer-aided detection of pulmonary embolism. *Scientific data*, 5(1): 1–9.
- McCann, M. T.; Nilchian, M.; Stampanoni, M.; and Unser, M. 2016. Fast 3D reconstruction method for differential phase contrast X-ray CT. *Optics express*, 24(13): 14564–14581.
- Moen, T. R.; Chen, B.; Holmes III, D. R.; Duan, X.; Yu, Z.; Yu, L.; Leng, S.; Fletcher, J. G.; and McCollough, C. H. 2021. Low-dose CT image and projection dataset. *Medical physics*, 48(2): 902–911.
- Nuyts, J.; Michel, C.; and Dupont, P. 2001. Maximum-likelihood expectation-maximization reconstruction of sinograms with arbitrary noise distribution using NEC-transformations. *IEEE transactions on medical imaging*, 20(5): 365–375.
- Shen, L.; Pauly, J.; and Xing, L. 2022. NeRP: implicit neural representation learning with prior embedding for sparsely sampled image reconstruction. *IEEE Transactions on Neural Networks and Learning Systems*.

- Su, T.; Cui, Z.; Yang, J.; Zhang, Y.; Liu, J.; Zhu, J.; Gao, X.; Fang, S.; Zheng, H.; Ge, Y.; et al. 2022. Generalized deep iterative reconstruction for sparse-view CT imaging. *Physics in Medicine & Biology*, 67(2): 025005.
- Szczykutowicz, T. P.; Toia, G. V.; Dhanantwari, A.; and Nett, B. 2022. A review of deep learning CT reconstruction: concepts, limitations, and promise in clinical practice. *Current Radiology Reports*, 10(9): 101–115.
- Willemink, M. J.; and Noël, P. B. 2019. The evolution of image reconstruction for CT—from filtered back projection to artificial intelligence. *European radiology*, 29: 2185–2195.
- Wu, W.; Hu, D.; Niu, C.; Yu, H.; Vardhanabhuti, V.; and Wang, G. 2021. DRONE: Dual-domain residual-based optimization network for sparse-view CT reconstruction. *IEEE Transactions on Medical Imaging*, 40(11): 3002–3014.
- Xu, K.; Lu, S.; Huang, B.; Wu, W.; and Liu, Q. 2024. Stage-by-stage Wavelet Optimization Refinement Diffusion Model for Sparse-View CT Reconstruction. *IEEE Transactions on Medical Imaging*.
- Yang, L.; Ge, R.; Feng, S.; and Zhang, D. 2022. Learning projection views for sparse-view ct reconstruction. In *Proceedings of the 30th ACM International Conference on Multimedia*, 2645–2653.
- Zhang, J.; Hu, Y.; Yang, J.; Chen, Y.; Coatrieux, J.-L.; and Luo, L. 2017. Sparse-view X-ray CT reconstruction with Gamma regularization. *Neurocomputing*, 230: 251–269.
- Zhu, B.; Liu, J. Z.; Cauley, S. F.; Rosen, B. R.; and Rosen, M. S. 2018. Image reconstruction by domain-transform manifold learning. *Nature*, 555(7697): 487–492.